Design Principles for Photovoltaic Devices Based on Si Nanowires with Axial or Radial p−n Junctions

Joseph D. Christesen, Xing Zhang, Christopher W. Pinion, Thomas A. Celano, Cory J. Flynn, and James F. Cahoon*

Department of Chemistry, University of North Carolina at Chapel Hill, Chapel Hill, North Carolina 27599, United States

S Supporting Information

ABSTRACT: Semiconductor nanowires (NWs) are a developing platform for electronic and photonic technologies, and many demonstrated devices utilize a p-type/n-type (p−n) junction encoded along either the axial or radial directions of the wires. These miniaturized junctions enable a diverse range of functions, from sensors to solar cells, yet the physics of the devices has not been thoroughly evaluated. Here, we present finite-element modeling of axial and radial Si NW p−n junctions with total diameters of ~240 nm and donor/acceptor doping levels ranging from 10^{16} to 10^{20} cm^{-3}. We evaluate the photovoltaic performance of horizontally oriented NWs under 1 sun illumination and

compare simulated current−voltage data to experimental measurements, permitting detailed analysis of NW performance, limitations, and prospect as a technology for solar energy conversion. Although high surface-to-volume ratios are cited as detrimental to NW performance, radial p−n junctions are surprisingly insensitive to surface recombination, with devices supporting open-circuit voltages (V_{OC}) of ~0.54 V and internal quantum efficiencies of 95% even with high surface recombination velocities (SRVs) of 10^5 cm/s. Axial devices, in which the depletion region is exposed to the surface, are far more sensitive to SRV, requiring substantially lower values of 10^3−10^4 cm/s to produce the same level of performance. For low values of the SRV (<100 cm/s), both axial and radial NWs can support V_{OC} values of >0.70 V if the bulk minority carrier lifetime is 1 μs or greater. Experimental measurements on NWs grown by a vapor−liquid−solid mechanism yield V_{OC} of 0.23 and 0.44 V for axial and radial NWs, respectively, and show that axial devices are limited by a SRV of ~7 × 10^3 cm/s while radial devices are limited by a bulk lifetime of ~3 ns. The simulations show that with further development the electrical characteristics of 200−300 nm Si NWs are sufficient to support power-conversion efficiencies of 15−25%. The analysis presented here can be generalized to other semiconductor homo- and heterojunctions, and we expect that insights from finite element modeling will serve as a powerful method to guide the design of advanced nanoscale structures.

KEYWORDS: *p−n junction, solar cell, photovoltaic, photodiode, Si nanowire, device simulation*
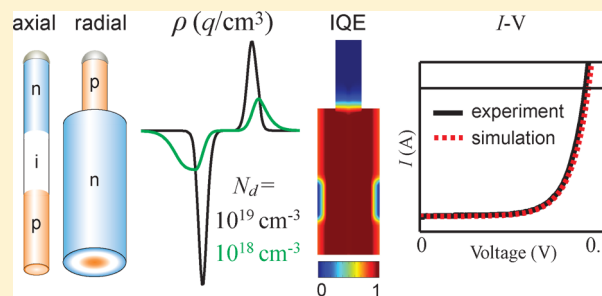
Semiconductor nanowire (NW) p-type/n-type (p−n) junctions represent a fundamental building block for the construction of advanced electronic and photonic devices based on single NWs. These junctions have been realized in a range of NW systems including Si,[1−9] InP,[10] GaN,[11] GaAs,[12,13] and CdS.[14,15] As illustrated in Figure 1A, two widely explored geometries are the axial junction, in which the p−n transition is encoded along the length of the wire, and the radial junction, in which the p−n transition is encoded from the center to outer surface, creating a core−shell geometry. Axial p−n junctions have permitted wires to be used as sensors,[16] photodiodes,[17] and photovoltaics[2,10] while radial junctions have primarily been used for photovoltaic devices.[1,3,11,12] Because of the ease of doping, integration, earth abundance, and relatively low cost, Si NWs have received special attention as an important new technology, especially for solar energy applications.[18−20] Compared with well-developed planar crystalline Si, wire-based Si structures could enable low-cost solar cells by

permitting high power-conversion efficiencies with relatively low-quality Si.[21]

Here, we use finite-element simulations to delineate the characteristics and theoretical performance of Si NWs with either axial or radial p−n junctions and with diameters limited to a few hundred nanometers. We compare our simulation results to experimental measurements on NWs synthesized by a vapor−liquid−solid (VLS) mechanism.[22] In these VLS-grown wires, axial p−n or p-type/intrinsic/n-type (p−i−n) junctions are encoded by in-situ doping of the wire during VLS growth.[2,8,10] For core/shell NWs, the radial junctions are encoded by additional in-situ doping of the shell, which is formed by a vapor−solid growth mechanism.[1,3] Our modeling evaluates realistic NW device geometries and accounts for the effects of degenerately doped Si and charge carrier recombi-

A

axial nanowire

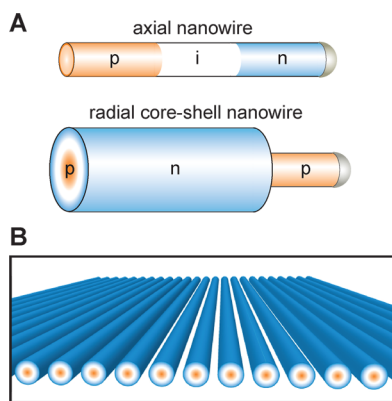radial core-shell nanowire

B

Figure 1. Overview of NW geometries used for photovoltaics. (A) Illustration of two distinct classes of NW p−n or p−i−n junctions that can be synthesized using vapor−liquid−solid (VLS) growth from a metal nanoparticle, including axial junctions (top) and radial junctions (bottom). (B) Schematic of NWs organized in a periodic horizontal array to form an ultrathin photovoltaic device.

nation by Shockley−Read−Hall (SRH), Auger, and surface recombination mechanisms.[23]

The wire-based solar cells considered here are composed of NWs oriented horizontally such that they are uniformly illuminated along their total length. To create a large-area solar cell, these wires can be arranged in a periodic array, as illustrated in Figure 1B. This topology is well-suited to take advantage of the optical resonances and photonic crystal effects that result from the subwavelength dimensions of the NWs and periodic arrangement, causing substantially enhanced light absorption.[1,24,25] An alternative implementation of Si wire-based solar cells uses arrays of vertically oriented wires that are several micrometers in diameter.[4,5,7,21] These vertical wire

arrays have been produced both by VLS growth[5,7] and by top-down etching of planar wafers or films.[4,9] The performance has been analyzed theoretically,[21,26] highlighting the benefit of collecting charge carriers over short, radial directions that are perpendicular to light propagation. The horizontal wires considered here operate in a different regime, in which the diameters are confined to subwavelength dimensions (200−300 nm) to take advantage of the optical effects in this geometry. Here, we address the device physics of these NWs to fully understand their potential as high-quality diodes and as wire-based thin-film photovoltaic devices.

The small size and geometry of NW p−n junctions is well-suited to finite element modeling that can accommodate arbitrary geometries and include a wide range of device physics parameters. The NWs were represented as a two-dimensional simulation domain with cylindrical symmetry (see Figure S1), which reduces computational cost but realistically represents the NWs as three-dimensional geometries. For each simulation point, we solved for the drift and diffusion of charge carriers in the presence of SRH, Auger, and surface recombination until converged stationary points were found. The simulations account for band gap renormalization in degenerately doped Si with the associated effects on built-in voltage and intrinsic carrier concentration.[23] Uniform optical generation of charge carriers was included to produce a short-circuit current density (J_{SC}) of 7 mA/cm² under 1 sun illumination[27] (except where noted otherwise), which is consistent with experimental measurement and with theoretical predictions of optical absorption in these structures.[24,25] Details of the device physics modeling are provided in the Supporting Information.

To define key characteristics determined by the geometry of the nanoscale p−n junctions, we examined the charge density and built-in electric fields for axial and radial NWs over a range of doping levels, as illustrated in Figure 2. To facilitate a direct
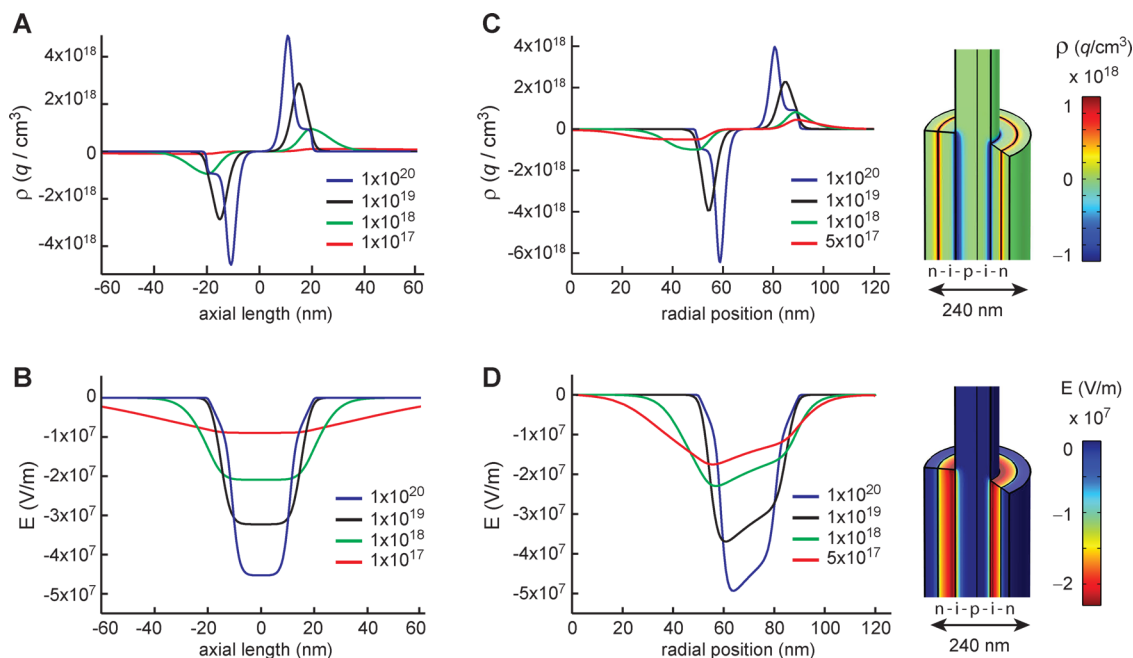
Figure 2. Charge density and electric field distributions for axial and radial NWs. (A) Charge density profiles in axial NWs for donor and acceptor doping levels of $10^{17}-10^{20}$ cm^{-3}. (B) Electric field profiles caused by the charge density distributions shown in panel A. (C) Charge density profiles (left) in radial NWs for donor and acceptor doping levels $5 \times 10^{17}-10^{20}$ cm^{-3}. Three-dimensional illustration (right) of the charge density distribution for 10^{18} cm^{-3}. (D) Profiles (left) and three-dimensional illustration (right) of the electric field generated by the charge density distributions shown in panel C.

comparison of the two geometries, both simulated structures possess a total diameter of 240 nm and include a ~40 nm intrinsic region between the n- and p-type regions. As expected, the doping level has a substantial effect on the space charge density and the electric field strength within the wires. For axial NWs (Figure 2A) with doping levels of 10^{18} cm^{-3} or greater, neither the n-type nor p-type regions reach full depletion. For instance, at 10^{20} cm^{-3}, the depletion region is at most 5% depleted, reaching a charge density of 5×10^{18} q/cm^3. For all doping levels, the electric field strength (Figure 2B) is on the order of 10^7 V/m, a value that is sufficiently high for carriers to reach saturation drift velocity in Si.[23]

For radial devices, we examined NWs with doping levels ranging from 5×10^{17} to 10^{20} cm^{-3}, as shown in Figure 2C,D. A detailed examination reveals several unique features. First, as observed in axial devices, the n- and p-type regions do not reach full depletion for doping levels greater than 10^{18} cm^{-3}. Second, the positive and negative charge distributions are asymmetric. For example, with a doping level of 10^{19} cm^{-3}, the negative charge density reaches a maximum value of ~4×10^{18} q/cm^3 while the positive side reaches only half the value, ~2×10^{18} q/cm^3. Third, the doping level of 5×10^{17} cm^{-3} produces a depletion region that extends to the center of the NW. Fourth, the electric field distributions (Figure 2D) are asymmetric, reflecting the asymmetry in the charge density distributions. The maximum electric field strengths increase with higher doping levels and, similar to axial devices, are on the order of 10^7 V/m.

The asymmetries present in the charge density and electric field distributions of the radial NWs result from the cylindrical symmetry of this junction. The magnitudes of both quantities are lower at larger radius because of the increasing volume per unit radius in the outer regions of the wire. This effect is especially pronounced at lower doping levels; below a doping level of 5×10^{17} cm^{-3}, the outer n-type shell retains a defined depletion region whereas the inner p-type core is fully depleted (see Figure S2). This effect prevents establishment of the full built-in potential drop across the junction, lowering the device performance and placing a lower limit on doping level that can be used in this structure.

To probe the photovoltaic characteristics of axial NW p−n junctions, we analyzed the performance of devices over a range of parameters, as presented in Figure 3. We have performed simulations with SRH minority carrier lifetimes (τ_{SRH}) ranging from $\tau_{SRH} = 10^{-10}$ to 10^{-6} s, which reflect varying mid-band-gap trap-state densities. Simulated current−voltage (I−V) curves[27] for $\tau_{SRH} = 10^{-8}$ s are displayed in Figure 3A, and photovoltaic metrics for a range of parameters are provided in Table S1. These I−V curves also include surface recombination velocities (SRVs) of $S = 0-10^5$ cm/s to account for a broad range of surface trap-state densities. Both short-circuit current (I_{SC}) and open-circuit voltage (V_{OC}) show a dramatic dependence on the SRV. From $S = 10^5$ to $S = 0$ cm/s, V_{OC} increases by 75% while I_{SC} increases by nearly 1 order of magnitude. The increase in I_{SC} results from a substantial increase in the internal quantum efficiency (IQE) of the wire, as discussed later. The increase in V_{OC} results from both the increase in I_{SC} and a reduction in charge carrier recombination within the depletion region, which is modulated by the SRV because of the direct exposure of the depletion region to the outer surface.

We systematically examine the effect of τ_{SRH} and SRV on V_{OC} in axial nanowires with a doping level 10^{18} cm^{-3} in Figure 3B. For a SRV of $S = 10^5$ cm/s, V_{OC} is limited to an upper value
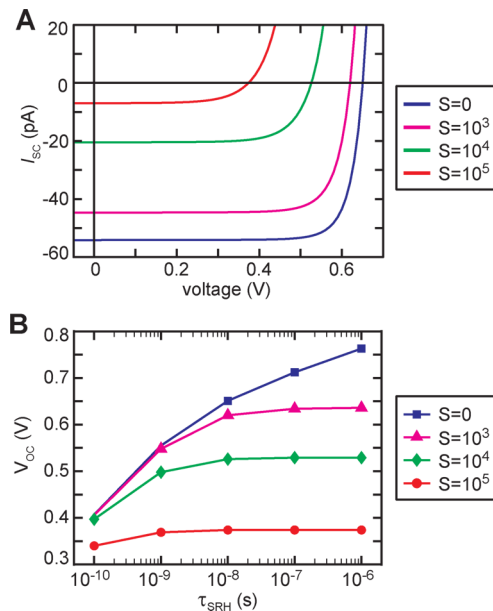

Figure 3. Analysis of axial p−i−n junction photovoltaic device characteristics. (A) Simulated I−V curves for axial NWs with a doping level of 10^{18} cm^{-3} and $\tau_{SRH} = 10^{-8}$ s. (B) V_{OC} versus minority carrier lifetimes of $\tau_{SRH} = 10^{-10}-10^{-6}$ s for a doping level of 10^{18} cm^{-3}. Simulations in panels A and B included SRVs of $S = 10^5$ (red), 10^4 (green), 10^3 (magenta), and 0 cm/s (blue).

of 0.37 V for all values of τ_{SRH}. For smaller values of SRV, increasing τ_{SRH} progressively increases V_{OC}, reaching a value of ~0.76 V for $S = 0$ cm/s and $\tau_{SRH} = 10^{-6}$ s. Surprisingly, this value exceeds the maximum V_{OC}, 0.71 V, reported for monocrystalline Si.[28] To understand this result, we can consider the expression for V_{OC} given by the Shockley diode equation:

$$V_{OC} \approx (nkT/q) \ln(I_{SC}/I_0) \qquad (1)$$

where n is the ideality factor, k the Boltzmann constant, T temperature, q electron charge, and I_0 the dark saturation current. As evident from this expression, V_{OC} is maximized by maximizing I_{SC} while simultaneously minimizing I_0. The axial geometry is uniquely suited to satisfy this condition because the small p−n junction area (defined by the NW cross-sectional area) minimizes I_0 while the long n- and p-type segments absorb light and maximize I_{SC}.

A similar analysis of the photovoltaic performance of radial NWs is presented in Figure 4. Current density−voltage (J−V) curves[27] for radial NWs with a doping level of 10^{18} cm^{-3} and τ_{SRH} ranging from 10^{-10} to 10^{-6} s are displayed in Figure 4A, and photovoltaic metrics for a range of parameters are listed in Tables S2 and S3. V_{OC} is dependent on both the τ_{SRH} and SRV, and the dependence of V_{OC} on these two parameters is plotted in Figure 4B. As expected, V_{OC} progressively increases with longer τ_{SRH} but, surprisingly, is relatively insensitive to the SRV for $\tau_{SRH} = 10^{-10}-10^{-8}$ s. For longer τ_{SRH} ($10^{-7}-10^{-6}$ s), however, V_{OC} shows a stronger dependence on SRV and is limited to a value of 0.54 V for $S = 10^5$ cm/s. With complete elimination of surface recombination ($S = 0$ cm/s), V_{OC} reaches a maximum value of 0.73 V at $\tau_{SRH} = 10^{-6}$ s.

We analyzed the power-conversion efficiency (η) of wires with doping levels of $10^{18}-10^{20}$ cm^{-3}. From the results over a range of τ_{SRH} and S (see Figure S4), a doping level of 10^{18} cm^{-3} maximizes efficiency. Higher doping levels exhibit reduced

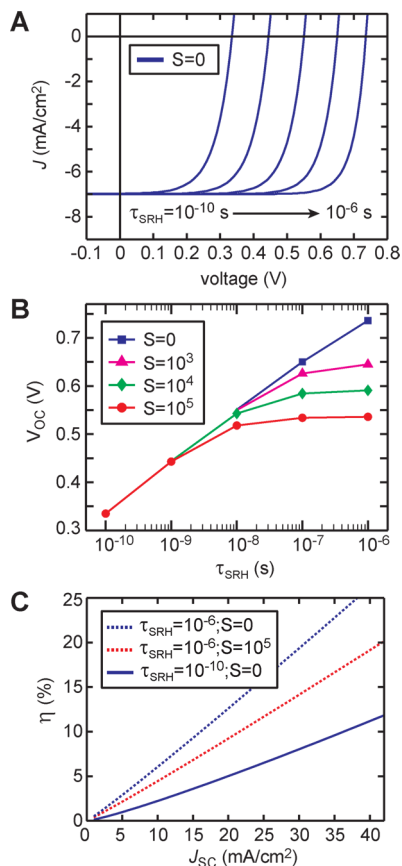**Figure 4.** Analysis of radial p−i−n junction photovoltaic device characteristics. (A) $J-V$ characteristics for radial wires with a doping level of 10^{18} cm^{-3} and $\tau_{SRH} = 10^{-10}-10^{-6}$ s, assuming a J_{SC} of 7 mA/cm^2 and SRV of $S = 0$ cm/s. (B) V_{OC} as a function of τ_{SRH} for a doping level of 10^{18} cm^{-3} and SRVs of $S = 10^5$ (red), 10^4 (green), 10^3 (magenta) and 0 cm/s (blue). (C) Power-conversion efficiencies (η) as a function of J_{SC} for wires with a doping level of 10^{18} cm^{-3} and with $\tau_{SRH} = 10^{-10}$ s (solid line) and 10^{-6} s (dashed lines) for SRVs of $S = 0$ (blue) and $S = 10^5$ cm/s (red).

Figure 5. Comparison of simulated and experimental $I-V$ or $J-V$ curves for single-NW photovoltaics under 1 sun illumination. (A) Experimental $I-V$ curve (black) for an axial VLS-grown p−i−n nanowire with a diameter of ∼160 nm and synthetically encoded intrinsic length of ∼2000 nm. Simulated $I-V$ curve (dashed red) was calculated using this experimental geometry, $\tau_{SRH} = 100$ ns, SRV of $S = 7 \times 10^3$ cm/s, and the experimentally measured J_{SC} of 4.8 mA/cm^2. (B) Experimental $J-V$ curve (black) for a radial p−i−n nanowire with a diameter of 260 nm composed of a VLS-grown p-type core of ∼100 nm diameter and intrinsic and n-type shell thicknesses of ∼45 and ∼35 nm, respectively. Simulated $J-V$ curve (dashed red) was calculated using $\tau_{SRH} = 3$ ns, SRV of $S = 10^5$ cm/s, and assuming the experimentally measured J_{SC} of 9.8 mA/cm^2.

efficiency primarily as a result of increased Auger recombination. Doping levels below 10^{18} cm^{-3}, on the other hand, fully deplete the p-type core as discussed earlier (see Figure S2).

The efficiency of radial NWs was determined for progressively increasing values of J_{SC} from 1 to 40 mA/cm^2, as illustrated in Figure 4C for $\tau_{SRH} = 10^{-10}$ and 10^{-6} s. Although experimental devices exhibited J_{SC} of only 7−10 mA/cm^2, further efforts to exploit light-trapping, photonic crystal, or plasmonic structures could be used to substantially enhance J_{SC} in these systems.[25,29] The simulation results demonstrate that the electrical properties of Si NWs are sufficient to support ultrathin solar cells with efficiencies in the range of 15−25%. Notably, a value of $\tau_{SRH} \sim 10^{-6}$ s can produce an efficiency >15% at a J_{SC} of 35 mA/cm^2 with poor surface passivation ($S = 10^5$ cm/s). Efficiency could be increased to >20% through elimination of surface recombination ($S = 0$ cm/s).

We synthesized axial and radial p−i−n NWs (see Supporting Information for methods) using a modification of literature procedures.[1,2] Measured $I-V$ and $J-V$ curves for axial and radial NWs under simulated 1 sun AM1.5G illumination are shown in Figures 5A and 5B, respectively, along with the best-fit simulations. The simulated and experimental $I-V$ curves without illumination (not shown) are well fit to the Shockley diode equation (eq 1), which can be used to extract n and I_0.
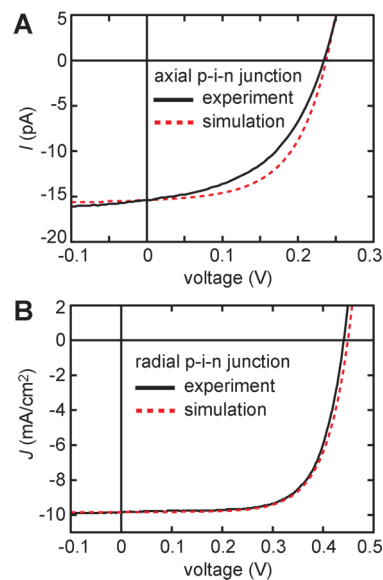
Note that the axial NW simulation geometry was adjusted to a diameter of 160 nm and intrinsic length of 2 μm to accurately reflect scanning electron microscopy images of the measured device. All experimental photovoltaic metrics are compared to the simulations of best fit in Table 1. For radial devices, a value of $\tau_{SRH} = 3$ ns and SRV of $S \leq 10^5$ cm/s reproduced the device parameters (V_{OC}, fill factor (FF), η, n, and I_0) from the core−shell p−i−n NWs. Similarly for axial devices, a value of $\tau_{SRH} \geq 5$ ns and a SRV of $S = 7 \times 10^3$ cm/s reproduced the measured device parameters. The good agreement of all metrics with experiment validates the use of finite-element simulations to analyze the performance of p−n junction NWs and to examine their prospect as a new class of ultrathin solar cell. Furthermore, the simulations demonstrate that the photovoltaic performance of axial devices is predominantly limited by surface recombination (S), whereas the performance of radial devices is limited by the bulk SRH recombination lifetime (τ_{SRH}). Because performance is limited by one parameter, we can at most place limits on the value of the other parameter—a lower limit $\tau_{SRH} = 5$ ns for axial and upper limit of $S = 10^5$ cm/s for radial devices.

As shown in Figure 6, we have examined the spatially dependent IQE of axial and radial NW junctions to understand the benefits and limitations of these geometries for efficient charge carrier collection. In axial NWs, the p-type, intrinsic, and n-type regions are each exposed to the outer surface. Within the depletion region, the IQE is >95% for SRVs of $S = 10^5$ cm/s and only drops to ∼80% with a SRV of $S = 10^6$ cm/s. Because the minority carrier diffusion length is much larger than the NW diameter, the IQE shows negligible radial dependence and instead decays exponentially along the length of the wire away

Table 1. Comparison of Experimental and Simulated Photovoltaic Metrics for Axial and Radial NWs

	τ_{SRH} (ns)	S (cm/s)	V_{OC} (V)	$J_{SC}{}^a$ (mA/cm^2)	FF	η (%)	n	I_0 (fA)
axial NW								
experiment			0.234	4.8	48	0.36	1.91	38
simulation	$\geq 5^b$	7×10^3	0.232	4.8	55	0.41	1.65	63
radial NW								
experiment			0.441	9.8	69	2.99	1.59	3.73
simulation	3	$\leq 10^{5\ c}$	0.449	9.8	69	3.03	1.84	3.75

^{a}Estimated using the intrinsic segment projected area for axial NWs and core−shell projected area for radial NWs. ^{b}Higher values produced similar photovoltaic metrics. ^{c}Lower values produced similar photovoltaic metrics.
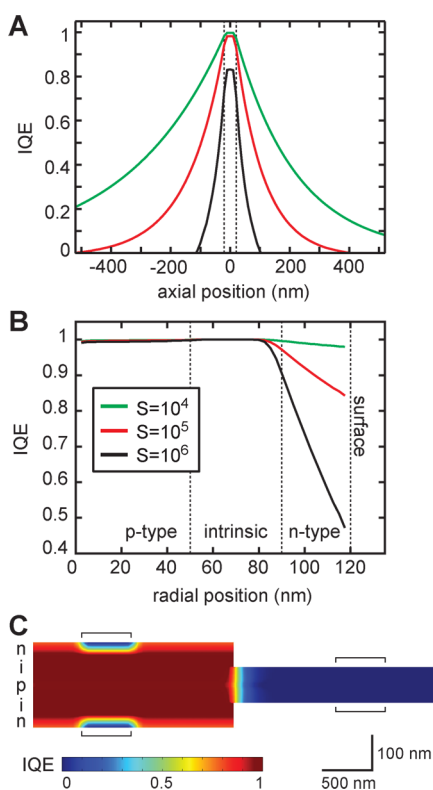

Figure 6. Internal quantum efficiency (IQE) of axial and radial NWs. (A) Radially integrated IQE as a function of axial position along an axial p−i−n NW with doping level of 10^{20} cm^{-3}, minority carrier lifetime of $\tau_{SRH} = 10^{-8}$ s, and SRVs of $S = 10^4$ (green), 10^5 (red), and 10^6 cm/s (black). (B) Axially integrated IQE as a function of radial position for a radial p−i−n NW with doping level of 10^{20} cm^{-3}, minority carrier lifetime of $\tau_{SRH} = 10^{-8}$ s, and SRVs of $S = 10^4$ (green), 10^5 (red), and 10^6 cm/s (black). (C) Spatial map of IQE for a radial p−i−n NW as shown in panel B with SRV $S = 10^5$ cm/s. Black bars indicate the positions of the Ohmic contacts.

from the depletion region. This decay is well fit to a monoexponential function (see Figure S5), which yields the effective minority carrier diffusion length, L_{eff}. It has been established that the L_{eff} is typically limited by the SRV rather than by the bulk minority carrier lifetime. Consequently, L_{eff} can be related to the diffusion constant D, minority carrier lifetime τ, S, and the NW diameter, d, as[8,30]

$$L_{eff} = \sqrt{D(1/\tau + 4S/d)^{-1}} \qquad (2)$$

For example, with $\tau = 10$ ns, $S = 10^5$ cm/s, and $D = 1.45$ cm^2/s, the electron L_{eff} from eq 2 is estimated to be 93 nm, which is in agreement with the fit to our simulation that yields a value of 96 nm (see Figure S5). Lower values of S produce substantially

larger values of L_{eff} and, consequently, higher values of I_{SC} (see Figure 3A and Figure S3A) as a result of high IQE values over a larger portion of the NW.

Unlike axial p−i−n devices, radial junctions possess buried p-type and intrinsic regions that are isolated from the wire surface. IQE as a function of radial position for a device with $\tau_{SRH} = 10^{-8}$ s is plotted in Figure 6B. Remarkably, the IQE is unity throughout the p-type and intrinsic regions and deviates from unity only in the outer 30 nm of the n-type region. For SRV of $S = 10^5$ cm/s, the IQE decays linearly from ∼100% at the edge of the depletion region to 84% at the outer surface, producing a high overall IQE of 95% for the entire core−shell region. Decreasing the surface recombination to $S = 10^4$ cm/s improves the overall IQE to 99%, and IQE at the surface is 98%. These results demonstrate the dramatic advantage of core−shell structures to produce high IQE values even with relatively high SRVs and low τ_{SRH}. In Figure 6C, we present a spatial map of IQE throughout the core and core−shell regions of a radial junction device with $S = 10^5$ cm/s. For the core−shell region, IQE is >80% except in the vicinity of the Ohmic contacts. For the core region, the IQE quickly approaches zero as result of surface recombination.

In conclusion, finite element simulations were used to evaluate the performance of axial and radial NW p−n junctions and to reproduce experimental measurements on these two NW structures. The simulations demonstrate that Si NW photovoltaic devices are capable of producing V_{OC} values of ∼0.7 V and could serve as the basis for thin-film solar cells with power-conversion efficiencies in the range of 15−25%. Radial wires show distinct advantages over axial wires, exhibiting high IQE values nearly independent of surface recombination. The experimental measurements suggest that axial structures are limited by surface recombination whereas radial structures are limited by a bulk minority carrier lifetime of ∼3 ns. For radial NWs, an improvement of the lifetime by ∼2 orders of magnitude would be sufficient to maximize the photovoltaic performance. These results provide motivation for the continued development of 200−300 nm diameter Si NW photovoltaic structures and demonstrate the utility of finite-element simulations to quantitatively evaluate and design NW p−n junctions.

■ ASSOCIATED CONTENT

Ⓢ Supporting Information

Description of the device physics modeling, summary of experimental methods, Figures S1−S5, and Tables S1−S3. This material is available free of charge via the Internet at http://pubs.acs.org.

■ AUTHOR INFORMATION

Corresponding Author
*E-mail: jfcahoon@unc.edu.

Notes
The authors declare no competing financial interest.

■ REFERENCES

(1) Kempa, T. J.; Cahoon, J. F.; Kim, S.-K.; Day, R. W.; Bell, D. C.; Park, H.-G.; Lieber, C. M. *Proc. Natl. Acad. Sci. U. S. A.* **2012**, *109*, 1407.

(2) Kempa, T. J.; Tian, B.; Kim, D. R.; Hu, J.; Zheng, X.; Lieber, C. M. *Nano Lett.* **2008**, *8*, 3456.

(3) Tian, B. Z.; Zheng, X. L.; Kempa, T. J.; Fang, Y.; Yu, N. F.; Yu, G. H.; Huang, J. L.; Lieber, C. M. *Nature* **2007**, *449*, 885.

(4) Garnett, E.; Yang, P. D. *Nano Lett.* **2010**, *10*, 1082.

(5) Putnam, M. C.; Boettcher, S. W.; Kelzenberg, M. D.; Turner-Evans, D. B.; Spurgeon, J. M.; Warren, E. L.; Briggs, R. M.; Lewis, N. S.; Atwater, H. A. *Energy Environ. Sci.* **2010**, *3*, 1037.

(6) Kelzenberg, M. D.; Turner-Evans, D. B.; Putnam, M. C.; Boettcher, S. W.; Briggs, R. M.; Baek, J. Y.; Lewis, N. S.; Atwater, H. A. *Energy Environ. Sci.* **2011**, *4*, 866.

(7) Kendrick, C. E.; Yoon, H. P.; Yuwen, Y. A.; Barber, G. D.; Shen, H. T.; Mallouk, T. E.; Dickey, E. C.; Mayer, T. S.; Redwing, J. M. *Appl. Phys. Lett.* **2010**, *97*, 143108.

(8) Mohite, A. D.; Perea, D. E.; Singh, S.; Dayeh, S. A.; Campbell, I. H.; Picraux, S. T.; Htoon, H. *Nano Lett.* **2012**, *12*, 1965.

(9) Lu, Y. R.; Lal, A. *Nano Lett.* **2010**, *10*, 4651.

(10) Heurlin, M.; Wickert, P.; Falt, S.; Borgstrom, M. T.; Deppert, K.; Samuelson, L.; Magnusson, M. H. *Nano Lett.* **2011**, *11*, 2028.

(11) Dong, Y.; Tian, B.; Kempa, T. J.; Lieber, C. M. *Nano Lett.* **2009**, *9*, 2183.

(12) Colombo, C.; Heibeta, M.; Gratzel, M.; Fontcuberta i Morral, A. *Appl. Phys. Lett.* **2009**, *94*, 173108.

(13) Gutsche, C.; Niepelt, R.; Gnauck, M.; Lysov, A.; Prost, W.; Ronning, C.; Tegude, F.-J. *Nano Lett.* **2012**, *12*, 1453.

(14) Tang, J.; Huo, Z.; Brittman, S.; Gao, H.; Yang, P. *Nat. Nanotechnol.* **2011**, *6*, 568.

(15) Fan, Z. Y.; Razavi, H.; Do, J. W.; Moriwaki, A.; Ergen, O.; Chueh, Y. L.; Leu, P. W.; Ho, J. C.; Takahashi, T.; Reichertz, L. A.; Neale, S.; Yu, K.; Wu, M.; Ager, J. W.; Javey, A. *Nat. Mater.* **2009**, *8*, 648.

(16) Jiang, Z.; Qing, Q.; Xie, P.; Gao, R.; Lieber, C. M. *Nano Lett.* **2012**, *12*, 1711.

(17) Yang, C.; Barrelet, C. J.; Capasso, F.; Lieber, C. M. *Nano Lett.* **2006**, *6*, 2929.

(18) Hochbaum, A. I.; Yang, P. D. *Chem. Rev.* **2010**, *110*, 527.

(19) Peng, K. Q.; Lee, S. T. *Adv. Mater.* **2011**, *23*, 198.

(20) Garnett, E. C.; Brongersma, M. L.; Cui, Y.; McGehee, M. D. *Annu. Rev. Mater. Res.* **2011**, *41*, 269.

(21) Kayes, B. M.; Atwater, H. A.; Lewis, N. S. *J. Appl. Phys.* **2005**, *97*, 114302.

(22) Schmidt, V.; Wittemann, J. V.; Senz, S.; Gosele, U. *Adv. Mater.* **2009**, *21*, 2681.

(23) Sze, S. M.; Ng, K. K. *Physics of Semiconductor Devices*, 3rd ed.; John Wiley & Sons, Inc.: Hoboken, NJ, 2007.

(24) Kim, S.-K.; Day, R. W.; Cahoon, J. F.; Kempa, T. J.; Song, K.-D.; Park, H.-G.; Lieber, C. M. *Nano Lett.* **2012**, *12*, 4971.

(25) Cao, L. Y.; Fan, P. Y.; Vasudev, A. P.; White, J. S.; Yu, Z. F.; Cai, W. S.; Schuller, J. A.; Fan, S. H.; Brongersma, M. L. *Nano Lett.* **2010**, *10*, 439.

(26) Wong, S. M.; Yu, H. Y.; Li, J. S.; Li, Y. L.; Singh, N.; Lo, P. G. Q.; Kwong, D. L. *IEEE Electron Device Lett.* **2011**, *32*, 176.

(27) External electric potentials were applied to 500 nm wide Ohmic contacts located on the n- and p-type regions, and the flux of charge carriers through these contacts was used to calculate the current or photocurrent at each applied voltage. Except where noted, the simulations included an ideal back surface field (BSF) that prevented charge carrier recombination at the Ohmic contacts. Without the BSF, the small simulation size yielded pronounced narrow-base diode effects that would not be significant in experiments with long (>10 μm) NW lengths. This type of finite-element device modeling requires an accurate representation of variables that change by orders of magnitude over nanometer length scales; thus, high-resolution grid points below 1 nm were used in areas involving a rapid change of values such as the depletion region and boundaries of the Ohmic contacts. These device physics simulations were implemented in the framework of the COMSOL Multiphysics software package (*COMSOL Multiphysics*, 4.2a; Comsol Inc.: Burlington, MA, 2011).

(28) Green, M. A.; Emery, K.; Hishikawa, Y.; Warta, W. *Prog. Photovoltaics* **2010**, *18*, 346.

(29) Atwater, H. A.; Polman, A. *Nat. Mater.* **2010**, *9*, 205.

(30) Allen, J. E.; Hemesath, E. R.; Perea, D. E.; Lensch-Falk, J. L.; Li, Z. Y.; Yin, F.; Gass, M. H.; Wang, P.; Bleloch, A. L.; Palmer, R. E.; Lauhon, L. J. *Nat. Nanotechnol.* **2008**, *3*, 168.